Performance evaluation of AHWR Flux Mapping System during Normal Operational Scenarios

Anupreethi B[a,*], Vidya Sagar Yellapu[b], Anurag Gupta[a,c], Umasankari Kannan[a,c], Akhilanand Pati Tiwari[a,d]

[a] Homi Bhabha National Institute, Mumbai 400 094, Maharashtra, India
[b] School of Computing and Engineering, University of Huddersfield, Huddersfield HD1 3DH, United Kingdom
[b] Department of Electrical and Electronics Engineering, SRKR Engineering College, Bhimavaram 534 204, Andhra Pradesh, India
[c] Reactor Physics Design Division, Bhabha Atomic Research Centre, Trombay, Mumbai 400 085, Maharashtra, India
[d] Knowledge Management Group, Bhabha Atomic Research Centre, Trombay, Mumbai 400 085, Maharashtra, India

*****Corresponding author e-mail address*: anupreethi@barc.gov.in*

Abstract

In large nuclear reactors, a number of appropriately distributed in-core neutron detectors are used for monitoring and control of neutron flux distribution in the core. In Advanced Heavy Water Reactor (AHWR) too, a set of 168 self-powered neutron detectors installed vertically at 6 locations in 28 in-core detector housing units has been proposed to be used. This configuration arrived at using the K-means clustering approach, has been found to reconstruct the core neutron flux distribution for a number of steady-state flux shapes. For practical application, in addition to steady-state, the optimized set of in-core detectors should provide reasonably accurate core monitoring for regular reactor operations as well. This paper investigates the accuracy characteristics of flux mapping using the proposed set of 168 in-core self-powered neutron detectors in the reconstruction of time-varying flux shapes encountered during normal reactor operations. Time-dependent flux shapes arising due to perturbations such as the movement of reactivity devices, refuelling and xenon spatial oscillations are considered for this study. Flux reconstruction is performed using the well-known flux synthesis method.

From the analysis, it can be observed that the proposed set of in-core detectors reliably reconstructs the flux distribution in the reactor even during the normal operational scenarios. The RMS error in mesh flux using 168 SPNDs and 35 eigenmodes is found to be less than 10% across all the operational scenarios considered.

Keywords: Flux Mapping System (FMS), Operational scenarios, SPNDs, AHWR, Flux reconstruction, Flux Synthesis Method, Eigenmodes

1. Introduction

In large-sized nuclear reactors, an online Flux Mapping System (FMS) is employed to monitor the neutron flux distribution and also to ensure that the derived parameters such as zonal powers and channel powers are well within the design limits. The online FMS uses either a mathematical model of the reactor or a set of precomputed flux shapes also called as modes, to determine the core neutron flux distribution from in-core detector readings, taken as input. The positioning of in-core detectors plays a major role and many earlier studies involved the use of evolutionary optimization algorithms such as Genetic Algorithm, Simulated Annealing, etc., to decide on the locations (Li et al., 2019; Peng et al., 2014; Terman et al., 2018). All these heuristic algorithms were dependent on the proper definition of the objective function.

In India, a heavy water moderated, boiling light water-cooled reactor, called Advanced Heavy Water Reactor (AHWR) is being designed with the objective of the utilization of thorium for power production. In this reactor, Self-Powered Neutron Detectors (SPNDs) housed in In-Core Detector Housing (ICDH) units are proposed to be used for online flux mapping. For optimization of the number of ICDH units, a data-driven approach using the K-means clustering algorithm has been proposed (Anupreethi et al., 2020). The procedure involved the use of in-core detector measurements of few reactor flux shapes to group the in-core detectors based on relative correlation. The in-core detectors within a cluster are strongly correlated and

this property is used to arrive at the number and locations of in-core detectors. Using the approach, the initial regularly spaced 104 ICDHs have been reduced to 28 ICDHs with 6 axially distributed SPNDs in each ICDH, giving a total of 168 SPNDs. Their effectiveness in flux reconstruction for a few steady-state scenarios of the reactor operation has been analysed and the Root Mean Square (RMS) error in mesh flux was found to be less than 10% (Anupreethi et al., 2020). These locations proved effective for reliable reconstruction of steady-state neutron flux.

For practical application in AHWR, it is important to assess the performance of the optimized in-core detector locations for normal operation of the reactor. The neutron flux shape in AHWR is subjected to variations due to asymmetrical movement of reactivity devices, xenon spatial oscillations and other perturbations such as refuelling which is envisaged to be carried out on power. Hence, the accuracy characteristics of flux reconstruction have been studied in these typical operational scenarios. Several algorithms exist in the literature for flux reconstruction. Among them, those commonly known are flux synthesis method (Hinchley and Kugler, 1974), Internal Boundary Condition method (Kim et al., 1991), and Combined Least Squares technique (Lee and Kim, 2003). The flux synthesis method uses the in-core detector measurements and a set of precomputed modes to perform the flux reconstruction while the other methods use the in-core detector measurements and reactor 3-D model to perform the flux reconstruction. The objective of this paper is to test the effectiveness of the proposed set of 168 SPNDs in the flux reconstruction for the AHWR in its practical operational scenarios. Flux reconstruction is performed using the flux synthesis method and the RMS error in mesh fluxes is used to quantify the effectiveness of flux reconstruction.

The rest of the paper is arranged as follows. A brief introduction to AHWR and the proposed flux mapping detectors is presented in Section 2. Theoretical background on Flux Mapping Algorithm based on the flux synthesis method is provided in Section 3. The procedure to

generate measurement signals and details of AHWR closed-loop control are discussed in Section 4. The description of the normal reactor operational scenarios considered for testing the effectiveness of flux reconstruction using the optimized set of in-core detectors is provided in Section 5. The performance study of flux reconstruction during normal operational scenarios is presented in Section 6. The paper concludes with a summary of work completed and future scope in Section 7.

2. Description of proposed Flux Mapping Detectors for AHWR

AHWR is a 920 MWth, vertical, pressure tube type, heavy water moderated, boiling light water-cooled natural circulation reactor (Sinha and Kakodkar, 2006). Out of the total 513 lattice locations, the vertical fuel assemblies are placed in 452 locations as shown in Fig. 1. Of the rest 61 locations, 37 locations have Shut Off Rods (SORs) and 24 locations have other reactivity control devices (8 each), namely, Regulating Rods (RRs), Absorber Rods (ARs) and Shim Rods (SRs). The physical dimensions of AHWR are large in comparison to the neutron migration length in the core, which makes the different regions in it neutronically loosely coupled. In view of this, monitoring and control of core neutron flux distribution are required on a continuous basis. It has been proposed to use Vanadium SPNDs for control and monitoring and flux mapping purposes (Yellapu et al., 2017). The placement of these SPNDs in the reactor plays a major role in the flux reconstruction.

A systematic procedure for the placement of in-core detectors has been evolved and reported earlier (Anupreethi et al., 2020). The procedure is schematically represented in Fig. 2. A large number of ICDH units were assumed to be located as shown in Fig. 2(a), so as to have an ICDH at every alternate interstitial lattice giving a total of 104 ICDH units with each ICDH unit containing 6 SPNDs distributed axially. K-means clustering algorithm was applied to a set of data containing in-core detector measurements corresponding to 55 different reactor steady

state flux shapes and the in-core detectors were grouped into a finite number of clusters based on Pearson correlation distance (Razak et al., 2014), as shown in Fig. 2(b). As the members of the clusters were strongly correlated, one in-core detector location was chosen from each cluster as an optimal ICDH location. By doing so, we were able to reduce 104 ICDH units to 28 ICDH units, as shown in Fig. 2(c). Each of these ICDH units contains 6 SPNDs axially distributed in it, as shown in Fig. 2(d), thereby giving a total of 168 SPNDs. These 168 SPNDs are numbered as follows: the detectors in the topmost axial layer (denoted by Z1) are numbered from 1 to 28. The detectors in layer Z2 are numbered from 29 to 56, in layer Z3 from 57 to 84, in layer Z4 from 85 to 112, in layer Z5 from 113 to 140 and finally in layer Z6 from 141 to 168. A closer look at Fig. 2(c) reveals that the ICDH units fall in three radial rings. The central ring contains four ICDH units, namely, 12, 13, 16, and 17. The middle ring contains eight ICDH units, i.e., 6, 7, 9, 10, 19, 20, 22, and 23. The outer ring contains 16 ICDH units, i.e., 1, 2, 3, 4, 5, 8, 11, 14, 15, 18, 21, 24, 25, 26, 27, and 28. This set of 168 in-core detectors is proposed to be used alongwith the flux mapping algorithm discussed in the next section for flux reconstruction during normal operational scenarios.

3. Flux Mapping Algorithm based on Flux Synthesis Method

The traditional flux synthesis method has been used in this work for neutron flux reconstruction (Hinchley and Kugler, 1974). As already mentioned, the algorithm combines the information from in-core detector measurements and a set of modes representing the nominal configuration of the reactor, to estimate the 3-D neutron flux. The modes are obtained by solving the steady-state neutron diffusion equation using the subspace iteration technique, carried out with the 3-D neutronics code ARCH (Gupta, 2012). The set of equations to be solved is represented in the form,

$$M\phi_n = \frac{1}{k_n} F\phi_n, \tag{1}$$

where the operator M represents the neutron loss (due to absorption, leakage, and scattering) and F the fission production. ϕ_n denotes the eigenmode of the reactor configuration corresponding to the eigenvalue k_n (Stacey, 2007). The application of the subspace iteration technique to a reactor model is discussed in detail in (Modak and Jain, 1996) and the same has been adopted here. With this technique, several eigenmodes can be computed simultaneously.

The basic set of eigenmodes contains fundamental and several higher eigenmodes computed for the nominal reactor configuration which is when all RRs are at 67% in, all ARs are at 100% in and all SRs are at 100% out positions. This reference set of eigenmodes is computed offline, stored and used as modes for reconstruction of all the operational scenarios (Anupreethi et al., 2019). In AHWR, higher order modes are excited following any perturbations in the reactor core and hence using them for reconstruction provides better neutron flux estimation. The number of modes should be large enough such that any operational scenario can be effectively represented by them (Xia et al., 2012).

Considering N_D in-core detectors and N_m number of modes, the flux values at the in-core detector locations can be represented in matrix form as,

$$\Phi_D = SA, \tag{2}$$

where Φ_D is a $N_D \times 1$ vector of in-core detector measurements of the operational scenario sampled at discrete time instants, S is a $N_D \times N_m$ rectangular matrix of in-core detector readings computed from the modes of the nominal reactor configuration at the in-core detector locations and A is an unknown $N_m \times 1$ vector of combining coefficients. Since the number of in-core detectors is greater than the number of modes used, the system becomes over-determined and a least-squares technique is applied to solve (2). Thus, we have,

$$A = (S^T S)^{-1} S^T \Phi_D. \tag{3}$$

The unknown combining coefficient vector A can be computed using linear solvers (Saad, 2011). Once A is computed, the flux at all the meshes can be estimated using the fundamental and higher order modes. It is important to note that the flux synthesis method is not a time-dependent method, therefore, the flux reconstruction is performed in a quasi-static manner, from the samples of the in-core detector readings collected at discrete time instants.

4. Generation of measurement signals and closed-loop control of AHWR

4.1 Generation of measurement signals during operational scenarios

The time-series data of in-core detector readings are generated by simulation of time-dependent core neutronics equations based on multi-point kinetics method to obtain the fluxes in meshes and then combining the values in the meshes surrounding the SPNDs. In the following, the mathematical model is described in brief. As depicted in Fig. 3, for mathematical modelling, the AHWR core is considered to be divided into 17 zones in the core region, 17 each in both top and bottom reflector regions similar to the core region and 8 zones in side reflector, giving a total of 59 zones (Shimjith et al., 2010; Yellapu et al., 2013). The equations describing the time variation of zonal neutron flux, delayed neutron precursors' concentrations, iodine concentration, xenon concentration, and speeds of RRs, given respectively as,

$$\frac{d\phi_h}{dt} = -\omega_{hh}\nu_h\phi_h + \sum_{k=1}^{N_h} \omega_{hk}\nu_h\phi_k + (\rho_h - \beta)\frac{\phi_h}{l_h} + \sum_{i=1}^{m} \nu_h \lambda_i C_{ih}\,, \tag{4}$$

$$\frac{dC_{ih}}{dt} = \frac{\beta_i \phi_h}{\nu_h l_h} - \lambda_i C_{ih}, i = 1,2,\dots,m, \tag{5}$$

$$\frac{dI_h}{dt} = \gamma_I \Sigma_{fh}\phi_h - \lambda_I I_h, \tag{6}$$

$$\frac{dX_h}{dt} = \gamma_X \Sigma_{fh} \phi_h + \lambda_I I_h - (\lambda_X + \sigma_{aX} \phi_h) X_h, \tag{7}$$

and

$$\frac{dH_l}{dt} = K_{RR}\, V_l, l = 1, \dots, N_{RR}, \tag{8}$$

will be solved to obtain the neutron flux values in the zones. In (4),

$$\rho_h = \rho_{hc} + \rho_{hX}, \tag{9}$$

$$\rho_{hc} = (\mu_1\, H_l + \mu_2)\ , \tag{10}$$

$$\rho_{hX} = \frac{-\sigma_{aX} X_h}{\Sigma_{ah}}, \tag{11}$$

$(h = 1,2, \dots, Z)$.

In the above set of equations (4) – (11), ϕ_h is the neutron flux in zone h; ω_{hk} denotes the coupling coefficients between the zone h and its neighbouring zone k; ω_{hh} denotes the self-coupling coefficient of zone h; v_h is the mean velocity of neutrons; N_h is the number of zones neighbouring the zone h; Z is the number of zones in the core region; ρ_h is the reactivity in zone h and it is expressed as the sum of reactivity of control rods, ρ_{hc}, and that of xenon, ρ_{hX}, as given by (9); β is the total fission fraction of delayed neutrons; l_h is the prompt neutron lifetime; λ_i is the decay constant of delayed neutron group i; C_{ih} is the delayed neutron precursor concentration of the group i in zone h; β_i is the fission fraction of delayed neutron group i; I_h is the iodine concentration in zone h; γ_I is the fractional yield of Iodine; Σ_{fh} is macroscopic fission cross-section in zone h; λ_I is the iodine decay constant; X_h is the xenon concentration in zone h; γ_X is the fractional yield of xenon; λ_X is the xenon decay constant; σ_{aX} is the microscopic absorption cross-section of xenon; H_l is the position of RR 'l'; V_l is the

control voltage applied to the drive of RR 'l'; N_{RR} is the number of RRs; the constants K_{RR} = 0.56, μ_1 = -21.604 × 10^{-6}, and μ_2 = 1440.311 × 10^{-6} (Shimjith et al., 2010).

Once the zonal fluxes are obtained, the flux values of the meshes in different zones are computed using a de-homogenization method. A detailed derivation of the method is available in (Yellapu et al., 2013). The transient value of flux at each mesh is given by the ratio of the transient to steady-state zonal flux, multiplied by the steady-state value of mesh flux, i.e.,

$$\phi_{jk} = \frac{\phi_h}{\phi_h^0}\phi_{jk}^0 \tag{12}$$

where ϕ_{jk} is the flux value of mesh k and vertical grid j; the superscript 0 indicates steady-state value.

The fuel assemblies in AHWR are housed in pressure tubes and placed in a square lattice of 22.5 cm × 22.5 cm. Hence, the AHWR core is modelled in Cartesian geometry with the lattice pitch of 22.5 cm in the X- and Y- directions and in the Z- direction a mesh spacing of 14.58 cm is used. The ICDH units are located in the interstitial space between the channels, such that each ICDH unit in the reactor is surrounded by 4 coolant channels. Each SPND approximately 30 cm in length, occupies two mesh lengths in the axial direction and therefore it is surrounded by 8 meshes. The response of SPND is obtained by diffusion coefficient weighted average of the fluxes of these 8 neighbours (Ezure, 1988) as

$$\phi_d(t_k) = \frac{\sum_{\mathrm{p}=1}^{N_s} D_p^d \phi_p^d(t_k)}{\sum_{\mathrm{p}=1}^{N_s} D_p^d} \tag{13}$$

where $\phi_d(t_k)$ denotes the neutron flux of d$^{\text{th}}$ detector; D_p^d denotes the diffusion coefficient corresponding to neighbouring mesh p of d$^{\text{th}}$ detector; N_s (usually 8) denotes the number of

meshes around the dth detector; $\phi_p^d(t_k)$ denotes the neutron flux corresponding to neighbouring mesh p of dth detector, and t_k denotes the time instant. Effect of coolant voiding and detector noise characteristics have not been considered in this paper. In AHWR, it has been proposed to use Vanadium SPNDs, the response of which is characterized by a large delay of the order of 300 s. Therefore, a dynamic compensation algorithm is employed (Mishra et al., 2013) to compensate for the lag in the measurement signal.

The multi-point kinetics or nodal method used to simulate the operational scenarios is validated with the finite difference method and the results are available in (Yellapu et al., 2013). As shown there, the values of mesh fluxes computed using the multi-point kinetics model are in good agreement with the values obtained from finite difference computations and the RMS error is less than 5%. Thus, within a considerable region of perturbation around the steady state operating point, the core average flux, fluxes at the in-core detector locations, and the in-core detector signals determined from the mesh flux values computed using the multi-point kinetics code are believed to be accurate enough.

4.2 AHWR closed loop control

Large reactors such as the AHWR are susceptible to xenon induced spatial oscillations. During normal reactor operation, xenon concentration reaches an equilibrium value corresponding to the operating power level. If there is any change, say a decrease in power level due to perturbation in the core, the dynamic characteristics are such that the xenon concentration first increases and then after several hours, it decreases to attain a new equilibrium. This may lead to oscillatory behaviour and the oscillations can be either in-phase or out of phase. During in-phase oscillations, the total power oscillates. On the other hand, in case of out-of-phase oscillations, the total power remains constant but the zonal powers oscillate. In-phase oscillations get noticed easily and are controlled through total reactor power control. However,

out-of-phase oscillations are difficult to detect and control. If such oscillations are left uncontrolled, the power produced in some channels may exceed design limits, affecting fuel integrity. Also, during on-power refuelling, the power in the coolant channel being refuelled undergoes deviation from its equilibrium value. As an immediate consequence of this, the zonal and total power also may vary. Such variations need to be controlled.

AHWR uses both total and zonal power control schemes to keep the out-of-phase oscillations caused due to xenon and perturbations in zonal and total power due to refuelling, under control. The voltage to drive of RR is computed based on the error in total power and zonal power, as

$$V_{RR}(i) = K_P(P - D) + K_T(P_i - D_i), \tag{14}$$

where $V_{RR}(i)$ is the voltage signal to the drive of the ith RR; P is the total reactor power; D is the demand power; K_P is the total power controller gain; P_i is the power in the zone having ith RR; D_i is the steady-state power in the zone having ith RR; K_T is the zonal power controller gain and $'i'$ stands for zones 2, 4, 6, 8 where RRs 1, 3, 5, 7 are present. The control gains K_P and K_T in (14) are designed so as to achieve stability and good transient response characteristics for both the total power control and zonal power control. However, for the purpose of our analysis, we have assumed K_P = 20 and K_T = 5 which yields a stable response.

5. Description of operational scenarios simulated

Three representative reactor operational scenarios, namely the movement of RRs, refuelling and xenon spatial oscillations have been chosen for simulation and generation of time-series data of SPND readings. Several combinations of these operational scenarios have been worked out and these are expected to cover the operational regimes of the FMS as they range from slow to fast perturbations. The operational scenarios are described in the following subsections.

5.1 Movement of regulating rods

As mentioned in Sec. 2, AHWR has been designed with 8 RRs (refer to Fig. 1) to perform the regulating function. They are banked into two groups. Out of these, 4 RRs of group 1 namely, RR #1, #3, #5 and #7 are considered for this simulation. At steady-state operation, these RRs are at 66.7% in, which constitutes their nominal positions. The movement of one or multiple RRs, which introduces small reactivity perturbations, has been simulated as described in the following. The closed loop control is assumed to remain ineffective, i.e., K_P and K_T in (14) are both set zero.

5.1.1 Movement of one RR: As shown in Fig. 4, at t =10 s, RR-1 is driven in by 4.17%, i.e., one axial mesh length from its initial nominal position of 66.7%. It is held in that position for a short duration and then it is driven out by the same distance. After a short duration, the RR-1 is driven out by 4.17% and then driven in so as to bring it back to the initial position corresponding to its nominal steady-state configuration (Ananthoju et al., 2016). The reactivity due to the control rod, computed using (9), reaches up to -0.09 mk during the first half cycle of movement. During the next half-cycle of movement, the reactivity reaches up to a maximum of 0.09 mk, as can be seen in Fig. 4. The change in core average flux with time is limited to 6.9% as shown in Fig. 5. The zone and mesh fluxes and subsequently in-core detector readings are computed using (12) and (13). In the total simulation time of 70 seconds, the in-core detector readings were sampled uniformly at one second interval, giving a total of 70 observations for each of the 168 in-core detectors. A similar analysis can be performed for the movement of any other RR. However, as all RRs have similar reactivity characteristics, the results obtained would be similar to those obtained in the case of RR-1 movement. The movement of one RR causes distortion in flux distribution, whereby the mesh fluxes in the vicinity of the RR undergoing movement, deviate from the average mesh flux.

5.1.2 Simultaneous in-phase movement of two RRs: Next, simultaneous in-phase movement of two RRs is simulated. Depending upon the set of RRs considered, 6 unique combinations,

namely, movement of RR-1 and 3, RR-1 and 5, RR-1 and 7, RR-3 and 5, RR-3 and 7, and RR-5 and 7 simultaneously would be possible. Fig. 4 shows the position of RRs with time. The total reactivity change produced by two RRs in this scenario has been maintained the same as that in the case of one RR movement. Therefore, two RRs are moved in or out by one half of an axial mesh length distance. Fig. 5 shows the resulting time variation of core average flux. The trend and maximum change from equilibrium value are almost identical to those in the case of one RR movement.

5.1.3 Simultaneous movement of three RRs: Simultaneous movement of three RRs by one-third of one axial mesh length is simulated and depending upon the set of RRs considered, 3 unique combinations, namely, movement of RR-1, 3 and 5, RR-3, 5 and 7, and RR-5, 7, and 1 would be possible. The total reactivity is maintained the same as that of movement of one RR scenario or two RRs scenario. In this case also, the core average flux variation is almost identical to that occurring in the case of one RR or two RRs movement.

5.1.4 Simultaneous in-phase movement of four RRs: Simultaneous in-phase movement of four RRs (RR-1, RR-3, RR-5 and RR-7) is simulated. To have a total reactivity change of 0.09 mk, which is the same as that in the case of movement of one RR, four RRs are moved in and out to cover one-fourth the distance of one axial mesh length, as shown in Fig. 4. It is observed that the flux perturbation is about 9%, but the time at which the maximum occurred has changed (Fig. 5). This is because the magnitude of the reactivity is smaller and the reactivity raise is slower.

5.1.5 Simultaneous out-of-phase movement of two RRs: Simultaneous out-of-phase movement of the RRs has been simulated. The RR-1 in zone 2 is driven as explained in Sec. 5.1.1. Simultaneously, RR-3 in zone 4 is driven at the same speed albeit in the opposite direction so as to maintain the reactor critical at all time instants. The total power remains constant with time but zonal powers may vary as depicted by plots shown in Fig. 6. As the

RR1, which is located in zone 2, is being withdrawn, the power in zone 2 will rise. Due to diffusion of neutrons from zone 2 to its neighbouring zones, the power levels in zones 8, 9, 10, 16, and 17 will rise too. The magnitude of the power rise will be more in the zones nearer to the zone in which RR movement occurs. Similarly, when the RR in Zone 4 is being inserted, the power in zone 4 will decrease. This will also cause decrease in the power in zones 5, 6, 12, 13, and 14. Power levels in zones 1, 3, 7, 11, and 15 will not experience any effect because of neutralizing effects of upward change expected due to rise in zone 2 power and downward change expected due to decrease in zone 4 power. Zone 2 and zone 6 (close to zone 4) experience opposite effects in zonal power due to the out-of-phase movement of RRs. In another simulation, RR-1 and RR-5 are moved simultaneously in opposite directions. In this case also, the total power remains unchanged but zonal powers vary with time as depicted in Fig. 7.

5.1.6 Simultaneous out-of-phase movement of four RRs: In case of this simulation, the RRs 1 and 3 that are present in zone 2 and 4 respectively are driven out simultaneously as in the case of two RRs simultaneous in-phase movement while the other two RRs, namely RRs 5 and 7 present in zone 6 and 8 respectively are driven in at matching speed so as to maintain the reactor critical. The total power remains unchanged but zonal powers vary as depicted in Fig. 8. In the second simulation in this category, RRs 1 and 5 move out simultaneously while RRs 3 and 7 move in at matching speed, resulting in zonal power variation as depicted in Fig. 9.

5.2 Refuelling operational scenario

The next operational scenario considered is a refuelling scenario as on power refuelling is envisaged in AHWR. The scenario is simulated as follows. First, defuelling is carried out, i.e., fuel from one of the fuel channels is removed. Subsequently, refuelling is carried out, i.e, fresh fuel is inserted in the channel. Defuelling introduces a negative reactivity of -0.5 mk in 1800 s while refuelling introduces a positive reactivity of 0.7 mk in 1800 s, as depicted in Fig. 10. This

refuelling reactivity, ρ_{rf} is added to the reactivity term in (8) and the corresponding zonal fluxes are computed using (4)-(7) and (11). The simulation is carried out for sufficiently long duration giving sufficient time for stabilization of the total power to the initial value. During the simulation, the positions of RRs are regulated as given by (14). The in-core detector readings are then generated from the de-homogenized mesh fluxes using (12). Since refuelling is a slow transient, sampling at 60 seconds interval is carried out, to give a total of 121 observations from SPNDs. The simulation of the refuelling scenario is carried out for 5 zones, namely zones 1, 2, 3, 10 and 11 marked as N1, N2, N3, N10 and N11 in Fig. 3.

The variation of zonal and core average fluxes with time is shown in Fig. 11, for refuelling of a coolant channel in zone 10 in which the maximum deviation of zonal powers is seen to occur. The zonal flux reduces with defuelling and then it increases with refuelling. Due to the controller action, fluxes in the neighbouring zones such as zones 2, and 11 vary only slightly while the flux in zone 3 remains unaffected. However, the core average flux deviates from its equilibrium value by approximately 0.5%. Similar variations in zonal fluxes are seen to occur in case of other four refuelling scenarios, i.e., refuelling in zone 1, 2, 3, and 11.

5.3. Xenon spatial oscillations

As stated earlier in Sec. 4.2, xenon spatial oscillations are kept under control by regulating the signal to RRs as given by (14). However, for analysis of xenon spatial oscillation, we have considered a situation where the total power is regulated throughout the simulation whereas the zonal power controller is phased in when a change in power in any one of the four quadrants from its steady-state power is more than 10%. The first quadrant consists of zones 2, 3, 10, 11, and one-fourth of zone 1, and the second quadrant consists of zones 8, 9, 16, 17, and one-fourth of zone 1. The third quadrant consists of zones 6, 7, 14, 15, and one-fourth of zone 1, and the fourth quadrant consists of the remaining zones. The simulation is performed as follows:

1. AHWR is initially assumed to be under steady-state operation at full power. The total power controller is active throughout the simulation, i.e., K_P = 20 is set.
2. After one hour into the simulation, a small disturbance is introduced for a short duration by the movement of RR-1 in Zone 2. RR-1 is driven in by 4.17% along the axial mesh length from its initial position of 66.7% and then brought back to the initial position to maintain the net reactivity nearly zero. During and post the disturbance, the total power regulation is active, i.e., K_P = 20, whereas the zonal power controller is kept deactivated by keeping K_T = 0. This introduces xenon spatial oscillations.
3. When the power in any of the quadrants deviates by 10% from its steady-state value, the value of K_T = 5 is restored. The voltage signals to RRs 1, 3, 5 and 7 are adjusted in accordance to (14) to maintain the total power constant. Also, the zonal power levels are brought back to their respective equilibrium values, and xenon spatial oscillations are brought under control.

The simulation is carried out for the duration of 45 hours. The variation of total reactor power with time is depicted in Fig. 12. It can be observed that except for a short time, subsequent to the initial perturbation at t = 1 h, the total power is maintained close to demand power whereas the quadrant power levels and zonal power levels, as depicted by plots in Fig. 13 and 14, deviate from their respective equilibrium values. After some time, i.e., t = 7.935 h, as one of the quadrants experienced a deviation in power from its equilibrium value by more than 10%, zonal power controller was phased in by restoring K_T = 5. In this case, 10% deviation in quadrant-3 power was observed. The variation in zonal average flux and xenon concentration for the zones in quadrant 3 takes place as shown in Fig. 14. It can be observed that xenon concentration changes with time and as a result, the flux in that zone varies in an out-of-phase manner. Post the introduction of the zonal power controller, the four RR positions were adjusted based on the deviation of zonal power, leading to variation of RR positions with time as shown in Fig.

15. From the plots, it is evident that after few cycles of oscillation, the total reactor power was stabilized by the zonal and total power controller. The average flux in zones 6, 14 and 15 are seen to have changed by around 10%, causing a deviation of 10% power in the third quadrant. Powers in other zones remain almost unaffected, during the transient.

Xenon spatial oscillations are often characterised in terms of principal tilts, among which those important for AHWR are the first azimuthal tilt, second azimuthal tilt and the first radial tilt. These are depicted schematically in Fig. 16, and defined as,

$$First\ azimuthal\ tilt = \frac{P_L - P_R}{P_L + P_R} \times 100\%, \tag{15}$$

$$Second\ azimuthal\ tilt = \frac{(P_{++} + P_{--}) - (P_{-+} + P_{+-})}{(P_{++} + P_{--}) + (P_{-+} + P_{+-})} \times 100\%, \tag{16}$$

$$Radial\ tilt = \frac{P_{inner} - P_{outer}}{P_{inner} + P_{outer}} \times 100\%, \tag{17}$$

where P_L is the power of the left half of the core; P_R is the power of the right half of the core as shown in Fig. 16(a); P_{++} is the power in the first quadrant of the core; P_{-+} is the power in the second quadrant of the core; P_{--} is the power in the third quadrant of the core; P_{+-} is the power in the fourth quadrant of the core, where the first, second, third and fourth quadrants are indicated as '++', '-+', '- -', and '+-' respectively in Fig. 16(b); P_{inner} is the power in the inner core; P_{outer} is the power in the outer core as shown in Fig. 16(c). In the first azimuthal mode, the power oscillates in opposite phases in the left and right halves of the reactor core whereas, in the second azimuthal mode, the sum of the opposite quadrant powers oscillates out of phase with the sum of powers in the remaining quadrants. Power in the centre oscillates out of phase with power in the rest of the core in the case of the first radial mode (Shimjith et al., 2013).

During the entire simulation duration of 45 hours, samples of in-core detector readings were generated at a periodic interval of 5 minutes and at a shorter intervals around the time of

perturbation and when zonal controller phases in, giving a total of 1334 observations for each of the 168 in-core detectors.

6. Performance of FMS during operational scenarios

The performance of FMS in flux reconstruction using the optimized set of 168 SPNDs for the reactor operational scenarios is now discussed. The time-series data of in-core detector readings obtained from simulations are used to perform flux reconstruction. The data at each time instant are processed using the flux mapping algorithm described in Sec. 3. Thirty five eigenmodes are found to be sufficient for flux reconstruction (Anupreethi et al., 2020). For a given scenario, the flux reconstruction results obtained from the use of 624 SPNDs and 35 eigenmodes are taken as the reference solution. The error in reconstruction is quantified based on the RMS error, ε_{RMS} and Maximum Absolute Error (MAE), ε_{MAE}, defined below (Anupreethi et al., 2020; Mishra et al., 2012).

$$\varepsilon_{RMS}(t_k) = \sqrt{\frac{1}{\mathrm{N}_{mes}} \sum_{\mathrm{i}=1}^{\mathrm{N}_{meshe}} \left[\frac{\phi_i(t_k) - \bar{\phi}_i(t_k)}{\bar{\phi}_i(t_k)} \times 100\right]^2} \quad \%\,, \tag{18}$$

$$\varepsilon_{MAE}(t_k) = max\left\{\frac{\left|\phi_i(t_k) - \bar{\phi}_i(t_k)\right|}{\phi_{av}(t_k)}\right\}\Bigg|_{i=1:\mathrm{N}_{meshes}} \times 100 \ \%\,. \tag{19}$$

In the above equations, $\bar{\phi}_i(t_k)$ is the reconstructed reference total flux of i[th] mesh, i.e., the flux reconstructed using 624 SPNDs; $\phi_i(t_k)$ is the reconstructed flux using a smaller number of SPNDs, i.e., 168 SPNDs contained in 28 ICDH units and N_{mesh} denotes the total number of fuel meshes. The core average flux ϕ_{av} is computed as

$$\phi_{av}(t_k) = \frac{\sum_{i=1}^{\mathrm{N}_{meshes}} \phi_i(t_k)\, V_i}{\sum_{i=1}^{\mathrm{N}_{meshes}} V_i}, \tag{20}$$

where V_i denotes the volume of the i[th] mesh.

As evident from (18) and (19), the values of ε_{RMS} and ε_{MAE} are computed at each time instant, t_k, for each operational scenario.

6.1 Performance during RR movements

The results of reconstructed neutron flux distribution during the operational scenarios involving movement of one or multiple RRs, simulated in accordance to the procedure given in Sec. 5.1 is presented first. In the case of movement of one RR, two RRs, three RRs, and four RRs (out-of-phase movement), as expected, the flux distribution becomes asymmetric. Simultaneous in-phase and out-of-phase movement of two adjacent RRs and simultaneous out-of-phase movement of two pairs of adjacent RRs (RR 1, 3 and RR 5, 7) in four RR movement scenarios are seen to introduce comparatively the highest asymmetric distribution of neutron flux in the core. RMS errors and MAE values of mesh fluxes obtained using 168 SPNDs, taking the flux values obtained with 624 SPNDs as reference have been computed and some significant observations are given in Tables 1(A) and (B). Table. 1(A) gives the maximum value of ε_{RMS} during the entire duration of simulation and the time instant at which it occurred for each RR operational scenario. Table. 1(B) gives the maximum value of ε_{MAE}, the location at which it occurred and the time instant at which it occurred. Along with this, the percentage of meshes in which ε_{MAE}<2.5%, 2.5% ≤ ε_{MAE} < 5%, and ε_{MAE}≥ 5% are also given. From Table 1(A), it is evident that overall ε_{RMS} in mesh flux for all RR movement scenarios is well within 3%. The error statistics provided in Table 1(B) indicates that in most of the meshes, ε_{MAE} is less than 7.5%. It is evident that 168 SPNDs can effectively reconstruct the flux distribution caused by small reactivity perturbation.

6.2 Performance during refuelling

The results of the reconstructed neutron flux distribution for all the refuelling cases are presented next. Fig. 17 shows the 3-D profile of reconstructed neutron flux in zone 10 during

refuelling of a coolant channel where the initial flux distribution, the flux distribution at the start of refuelling and that at the end of refuelling have been shown. On defuelling, the flux drops below the initial level and on refuelling, it rises above the initial value. The error in flux reconstruction using 168 SPNDs, treating that with 624 SPNDs as reference has been estimated during refuelling.

Table 2(A) shows the flux reconstruction results in terms of ε_{RMS} and Table 2(B) shows the frequency distribution of ε_{MAE} in all fuel meshes, the magnitude of maximum ε_{MAE}, and the mesh in which the error is maximum. The maximum ε_{RMS} is found to be less than 5% for all the refuelling cases, establishing that 168 SPNDs can reliably reconstruct flux during refuelling. The maximum \epsilon MAE is found to be large as it is around 17 % but such large errors in mesh fluxes do not represent much concern as the corresponding thermal design margins are generally much larger than these.

6.3 Performance during xenon spatial oscillations

At each time instant during the simulation of xenon spatial oscillation as described in Sec. 5.3, the flux reconstruction has been carried out using 168 SPNDs and error in flux reconstruction is determined. The tilts caused are shown in Fig. 18. The first and second azimuthal tilts are dominant in AHWR. Within 7.9 hours, the first and second azimuthal tilts grow to amplitudes of the order of 3.89% and 0.073% respectively. The first radial mode is seen to oscillate as well, though the amplitude of oscillation is small. With phasing in of zonal power controller, the tilts are suppressed after few cycles of oscillation. The maximum absolute error in flux reconstruction in the case of xenon oscillations is shown in Table. 3. It can be seen that ε_{MAE} is less than 5% for the majority of meshes. Fig. 19 shows the time variation of ε_{RMS} which is high during the time when the quadrant power deviation exceeds 10% and the zonal controller is switched on. Few more peaks are also seen in the plot of azimuthal tilts shown in Fig. 18 but these peaks have much smaller magnitudes.

A 10% increase in total power could result in the shutdown of the reactor, however, the RMS error is computed for the mesh level. The tolerance for the change of total power with respect to mesh is high. Therefore, consideration of RMS error less than 10% as a design consideration is acceptable. From the study on the performance of FMS, it is evident that with the use of the optimized set of 168 in-core detectors, the normal reactor operational scenarios such as movement of RRs, refuelling and xenon spatial oscillations were reconstructed with ε_{RMS} less than 10% and hence, can effectively reconstruct the spatial flux variations.

7. Conclusion

In large reactors such as AHWR, it is important to assess the performance of FMS for reliable monitoring of normal reactor operations. FMS is used to determine the neutron flux distribution in the core. It depends on measurement signals coming from in-core detectors and a set of eigenmodes obtained from detailed off-line reactor physics computations. Our earlier work reported the use of K-means clustering approach to optimize the in-core detector locations in AHWR. By doing so, the initial set of regularly spaced 104 ICDH units containing 624 SPNDs was reduced to a set of only 28 ICDH units containing 168 SPNDs. These locations were tested for steady-state operation of the reactor and were able to reliably reconstruct the core flux. However, for practical application in AHWR, this set of optimized in-core detector locations should provide core monitoring for normal reactor operations with good accuracy.

In this paper, we investigated few reactor operational scenarios such as movement of regulating rods, refuelling and xenon spatial oscillations, resulting in perturbation in flux shape around the steady-state core flux distribution to test the effectiveness of flux mapping with the optimized set of 168 SPNDs. Using the simple flux synthesis method along with eigenmodes of nominal reactor configuration, flux reconstruction has been carried out to obtain the detailed neutron flux distribution in the core. Comparison of the results with the reference data

generated using a much larger number of detectors has been carried out. Specifically, the root means square error, as well as the maximum absolute error, were determined at various time instants during the operational scenarios considered. The maximum RMS error across all operational scenarios is found to be less than 10% while the maximum absolute error remained less than 16%, based on which it can be stated that the optimized set of 168 in-core detectors installed in 28 ICDH units can reliably reconstruct the spatial flux variations.

Further studies on the effect of failures of single or multiple in-core detectors on flux reconstruction could be done. It will also be interesting to explore the characteristics of various methods in recovering the signals of failed in-core detectors in a number of postulated situations. The effect of in-core detector noise characteristics on neutron flux reconstruction could be explored. Information theory can be applied to determine the redundancy of in-core detectors in the AHWR.

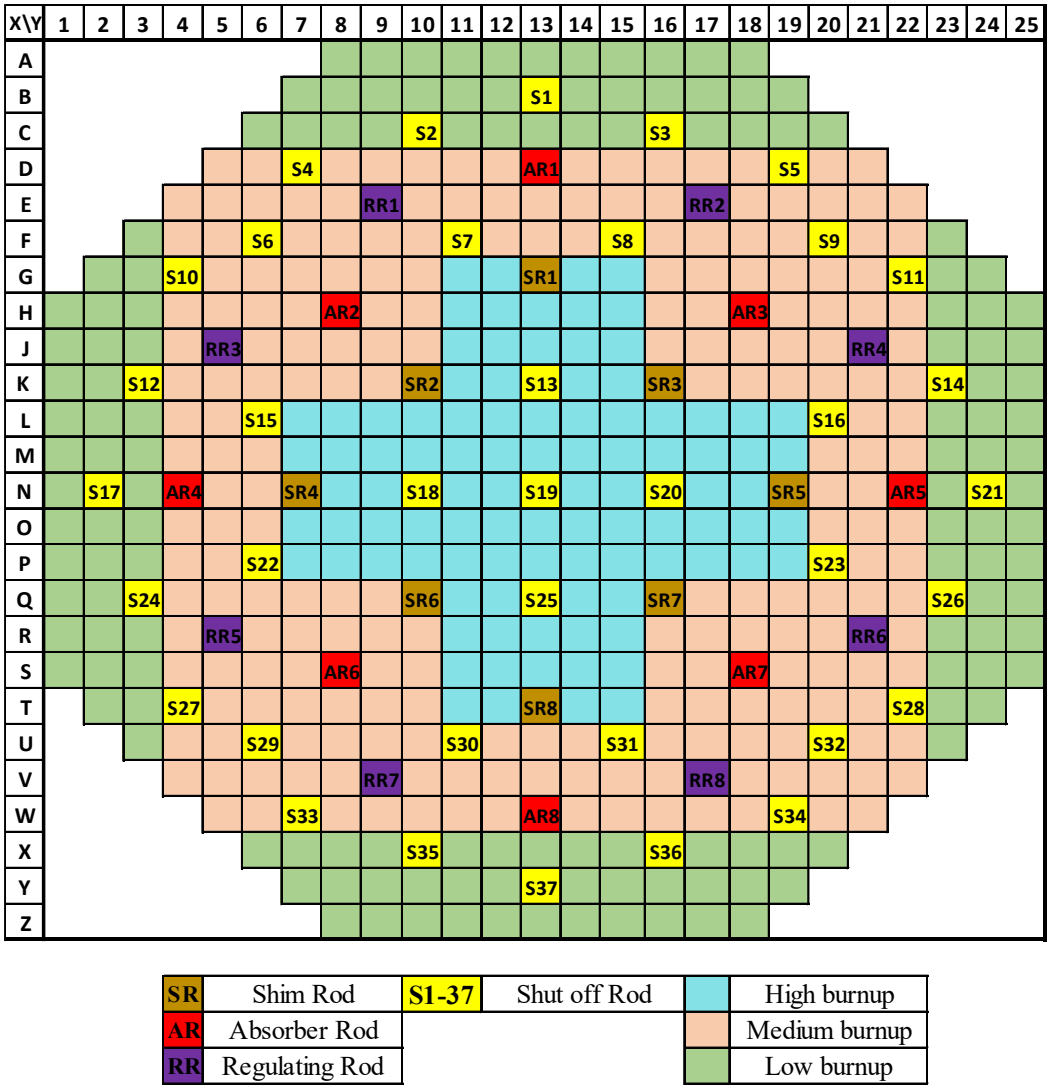

Fig. 1. AHWR core layout

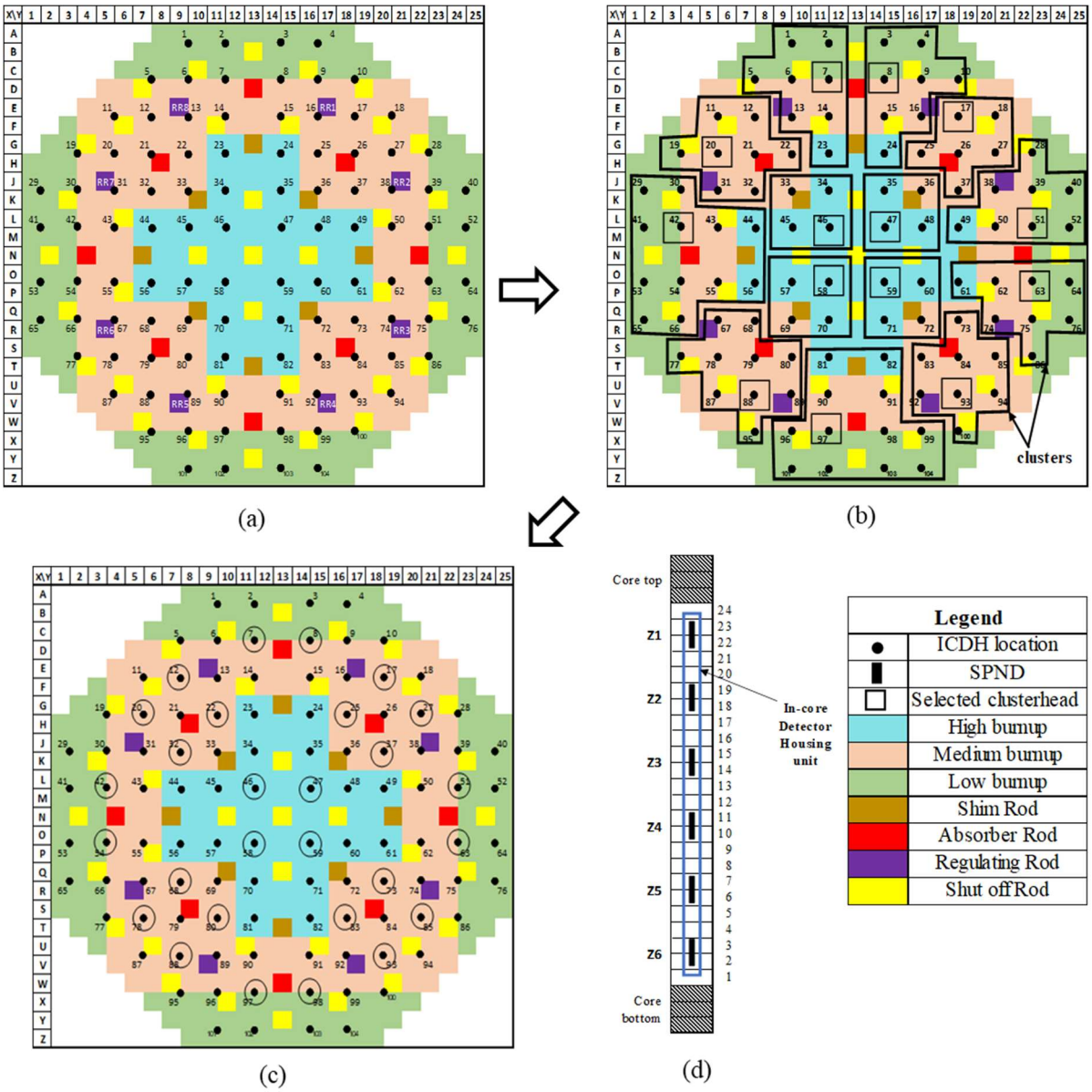

Fig. 2. Schematic representation of the procedure for in-core detector optimization in AHWR (a) Distribution of initial 104 ICDH units, (b) Application of *K*-means clustering and cluster formation, (c) Distribution of final optimized 28 ICDH units, and (d) Distribution of 6 SPNDs in each ICDH unit.

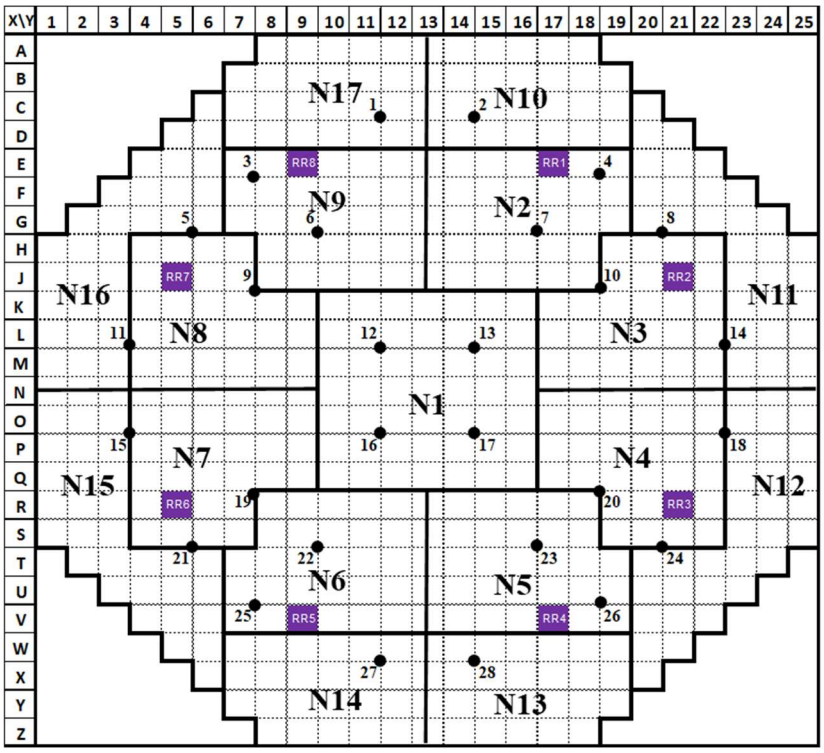

Fig. 3. Zonal configuration of AHWR with 17 zones in it. Zones are numbered as N1, N2, etc,

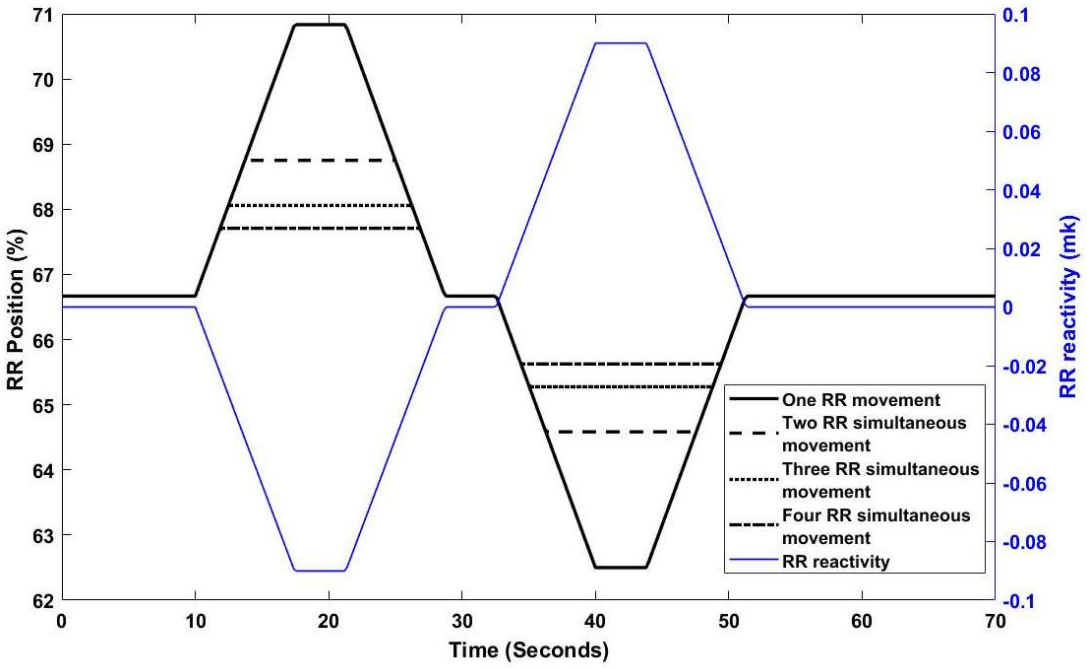

Fig. 4. RR position variation and its reactivity with time (Movement of one RR in each case is displayed)

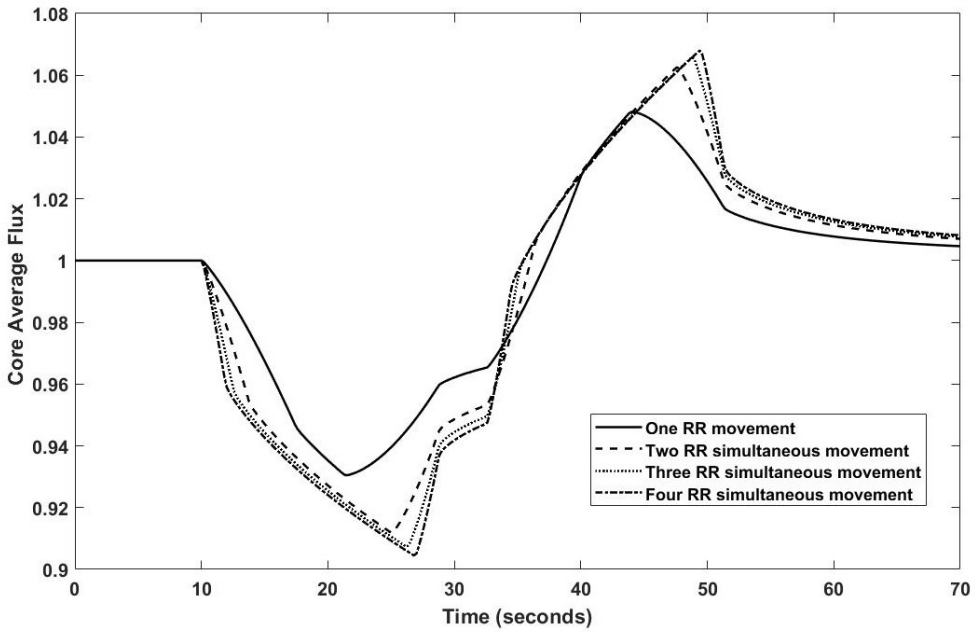

Fig. 5. Variation of core average flux with time for all simultaneous RR cases

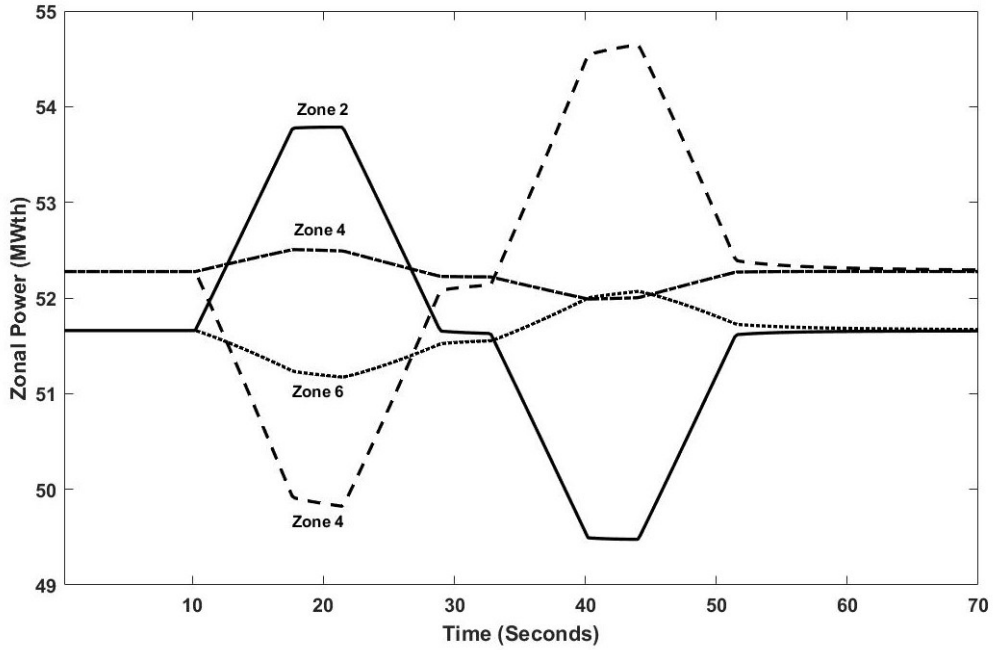

Fig. 6 Zonal power variation with time during out-of-phase simultaneous movement of RR1 and 3

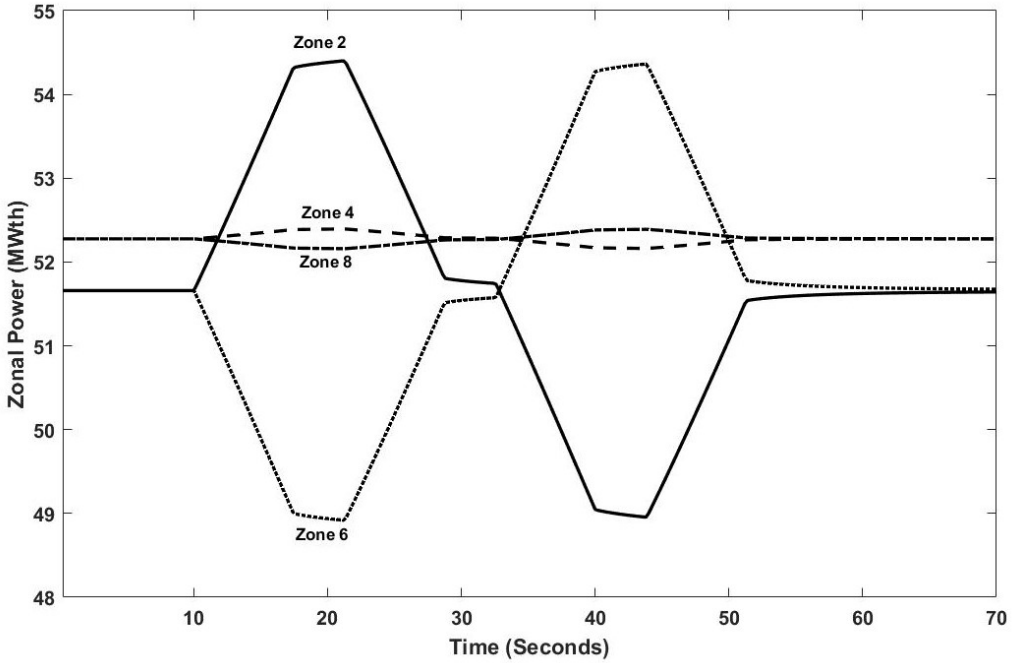

Fig. 7 Zonal power variation with time during out-of-phase simultaneous movement of RR1 and 5

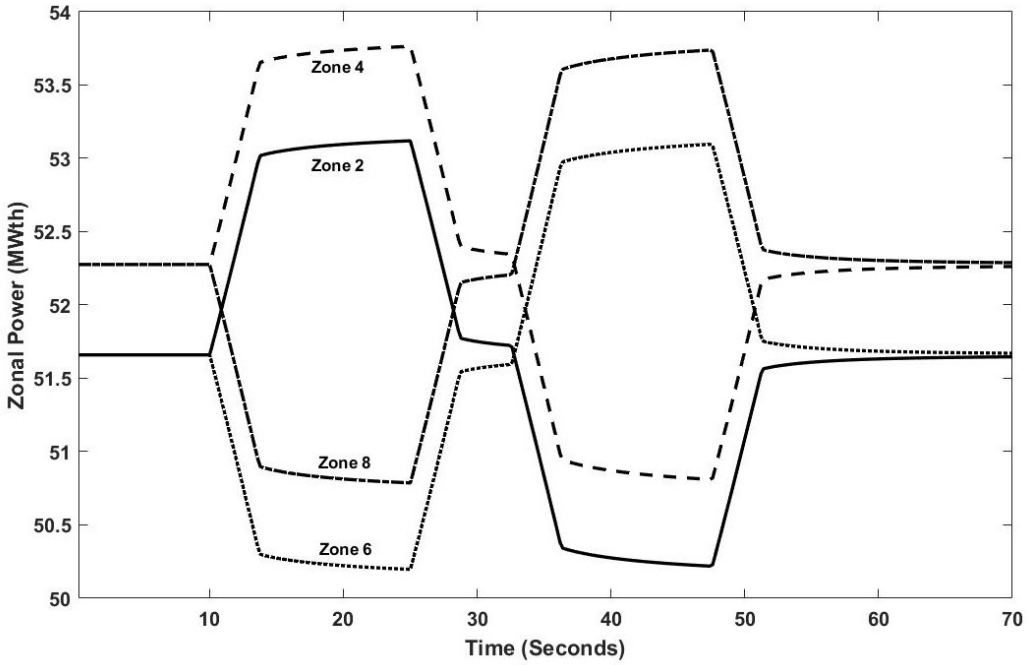

Fig. 8 Zonal power variation with time during out-of-phase simultaneous movement of four RRs - RR1, 3 moving out and RR5, 7 moving in during first half cycle and then RR1, 3 moving in and RR5,7 moving out in the next half cycle

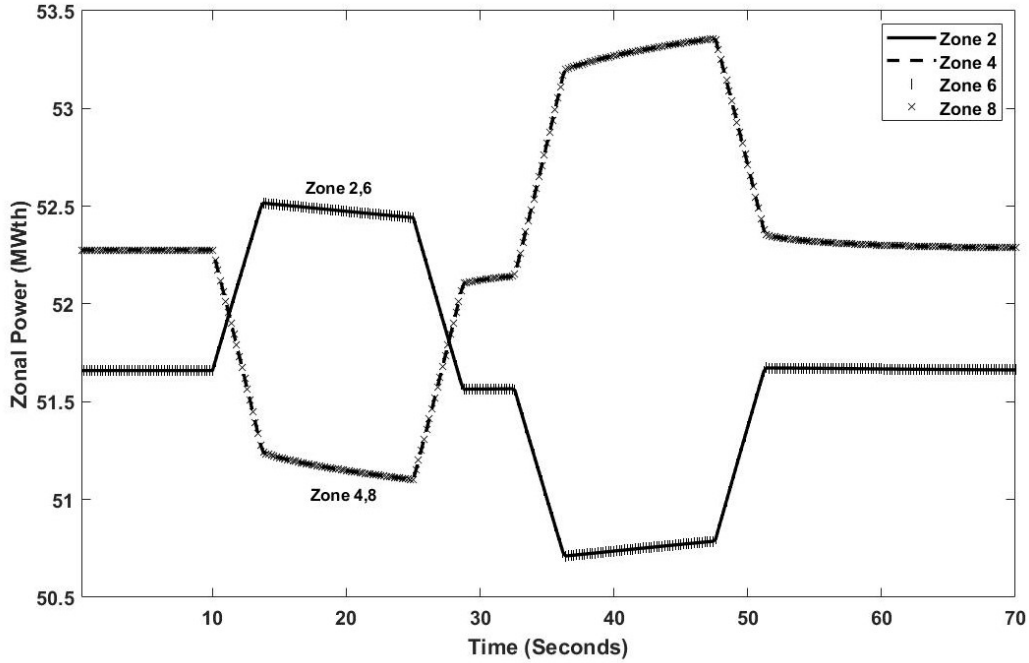

Fig. 9 Zonal power variation with time during out-of-phase simultaneous movement of four RRs - RR1, 5 moving out and RR3, 7 moving in during first half cycle and then RR1, 5 moving in and RR3, 7 moving out in the next half cycle

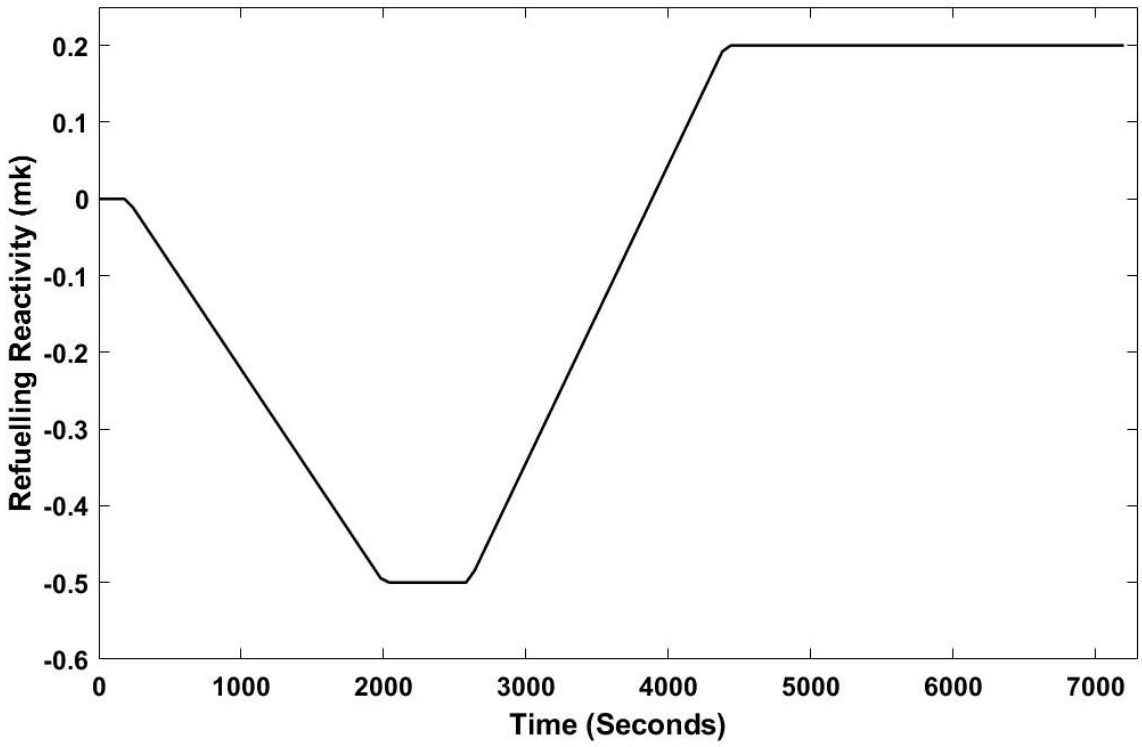

Fig. 10. Reactivity variation during refuelling of a coolant channel in the zones

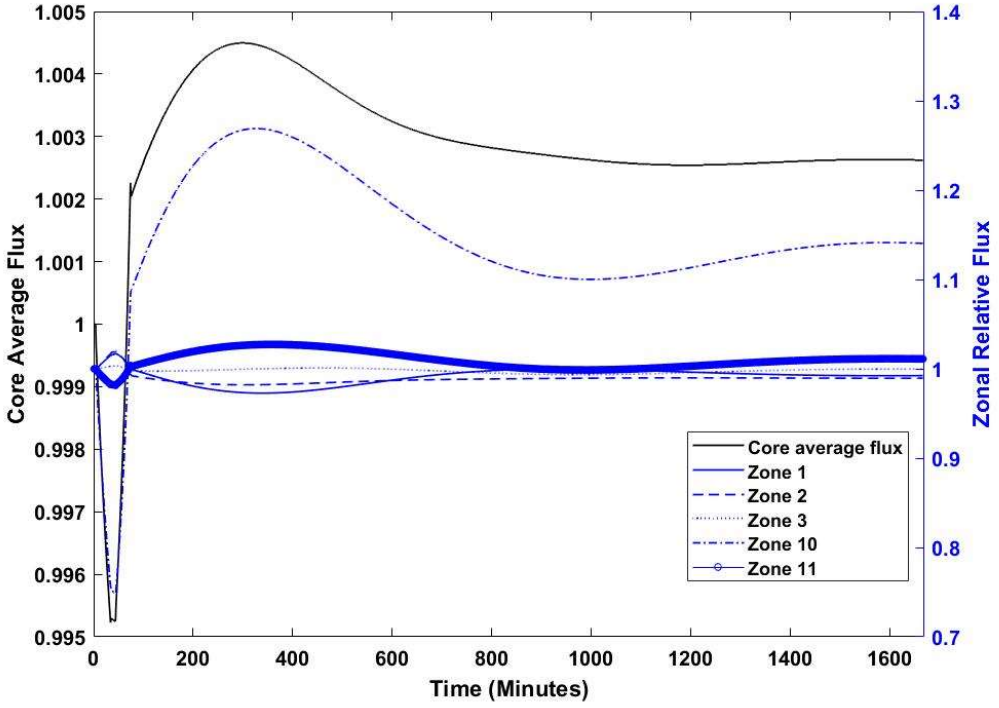

Fig. 11. Variation of core average and zone 1, 2, 3, 10 and 11 fluxes with time during refuelling of a coolant channel in Zone 10

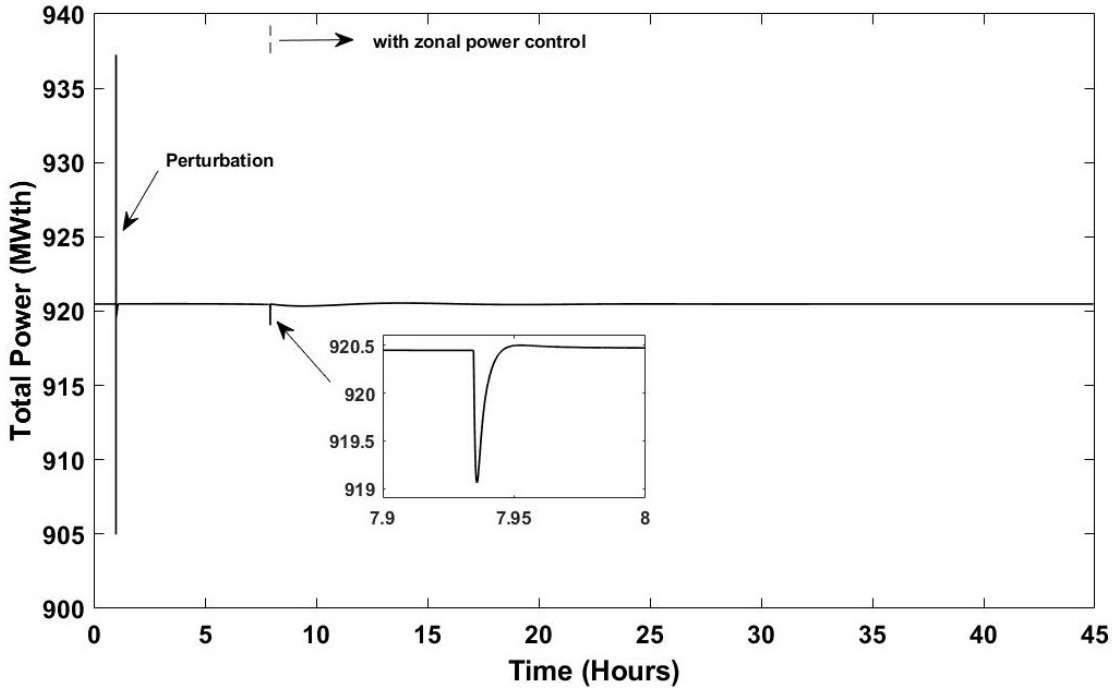

Fig. 12. Variations in total reactor power with time (The inset box shows a portion of the plot zoomed)

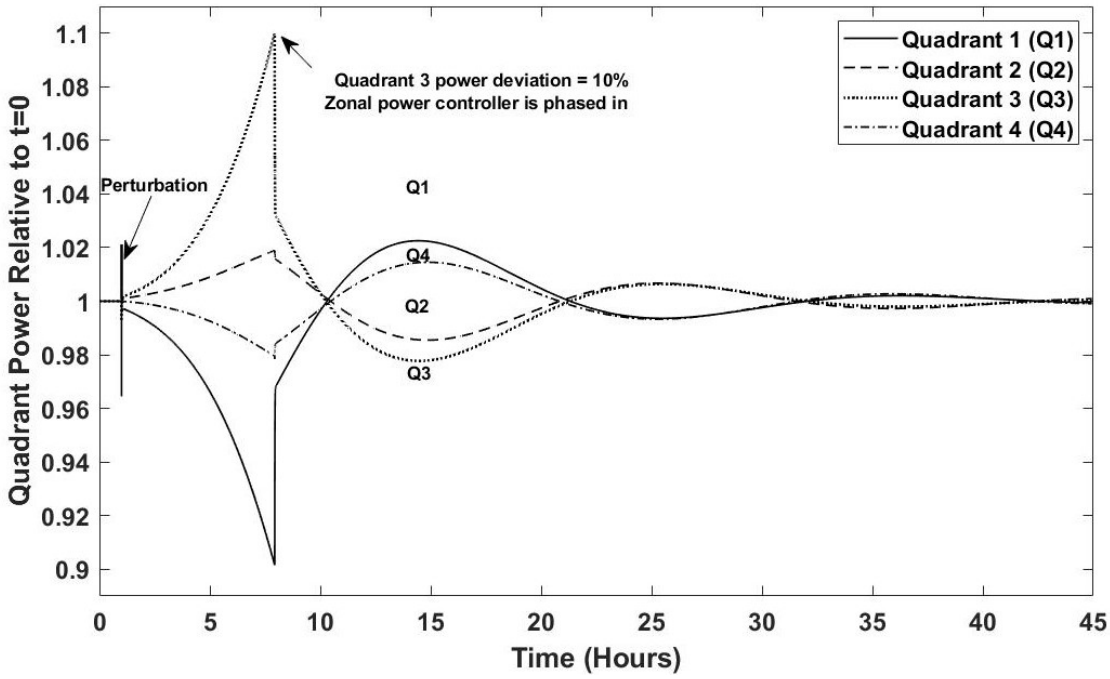

Fig. 13. Variation of quadrant powers with time

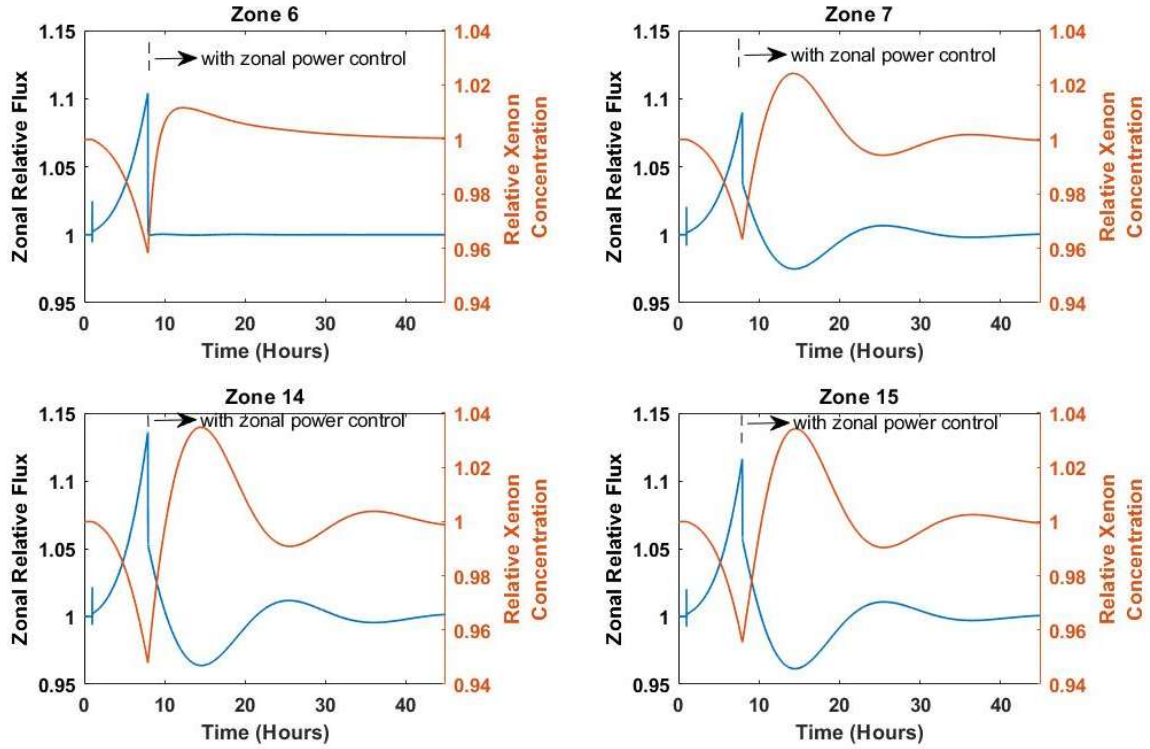

Fig. 14. Variation of zonal average flux and relative xenon concentration for the zones present in Quadrant 3

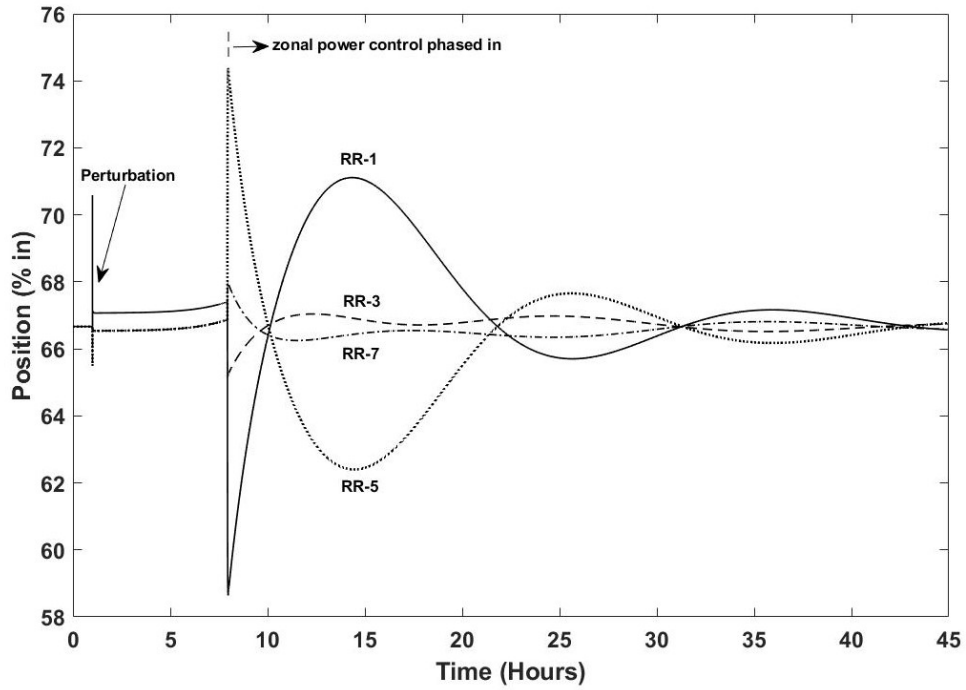

Fig. 15. Variation of positions of RRs 1, 3, 5, and 7 with time

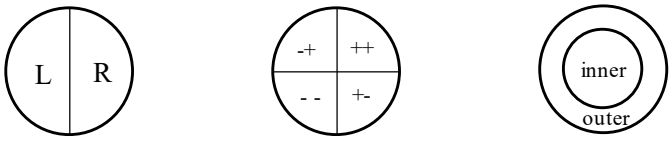

(a) (b) (c)

Fig. 16. Schematic representation of principal tilts in AHWR (a) First azimuthal (b) Second azimuthal, and (c) First radial

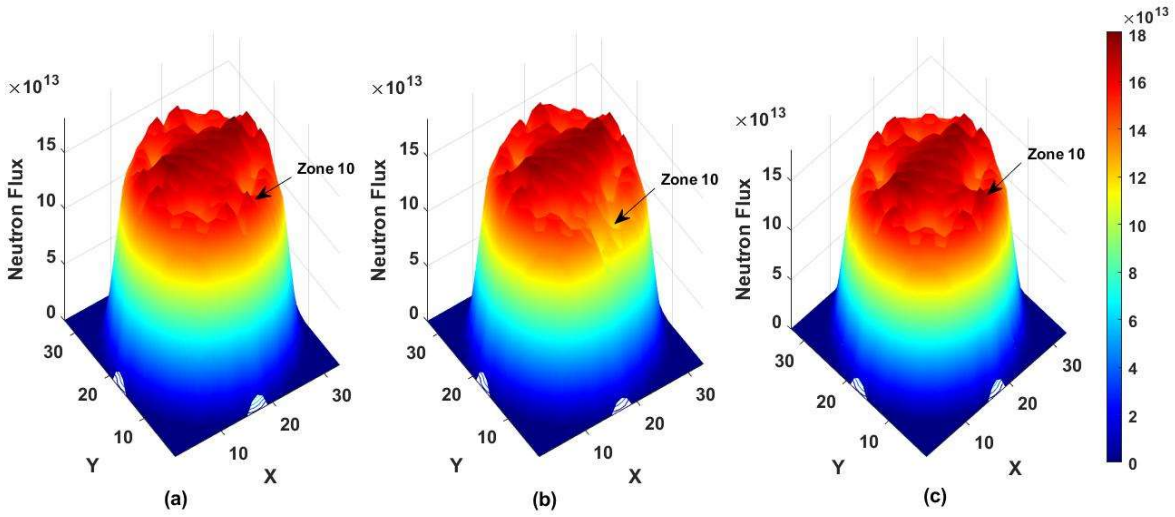

Fig. 17. 3-D reconstructed neutron flux distribution for refuelling of a coolant channel in zone 10 – (a) initial state (b) t = 2520 s, start of refuelling (c) t = 4380 s, end of refuelling.

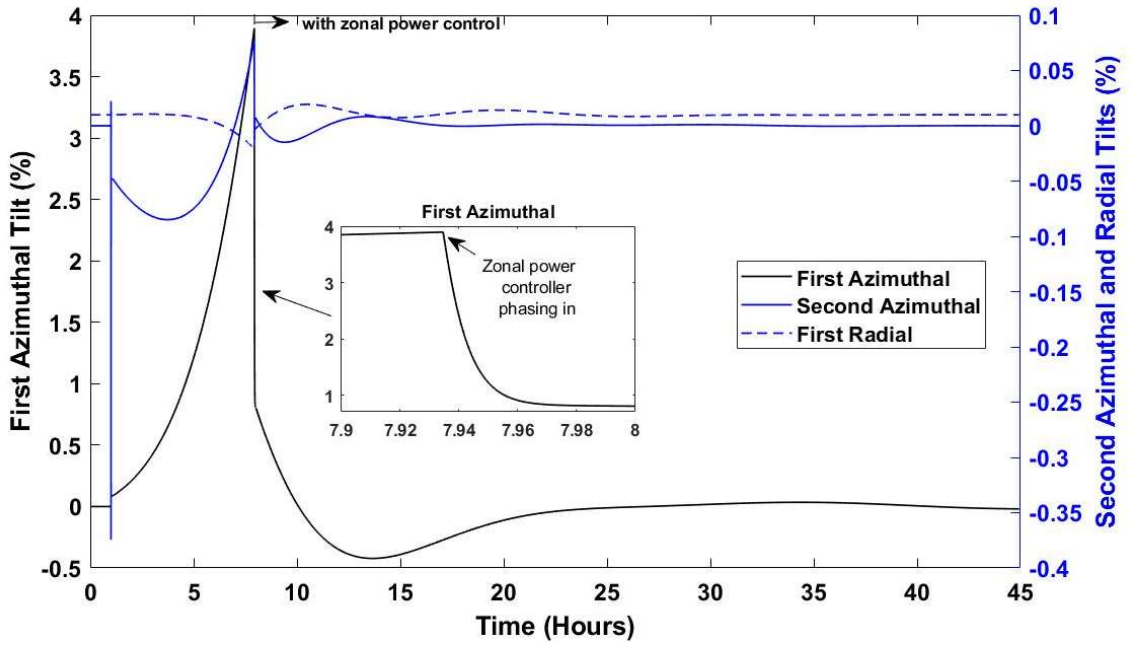

Fig. 18. Variation of first azimuthal, second azimuthal, and radial tilts during xenon spatial oscillations (portion of plot between 7.9 hours and 8 hours is shown zoomed in the inset box)

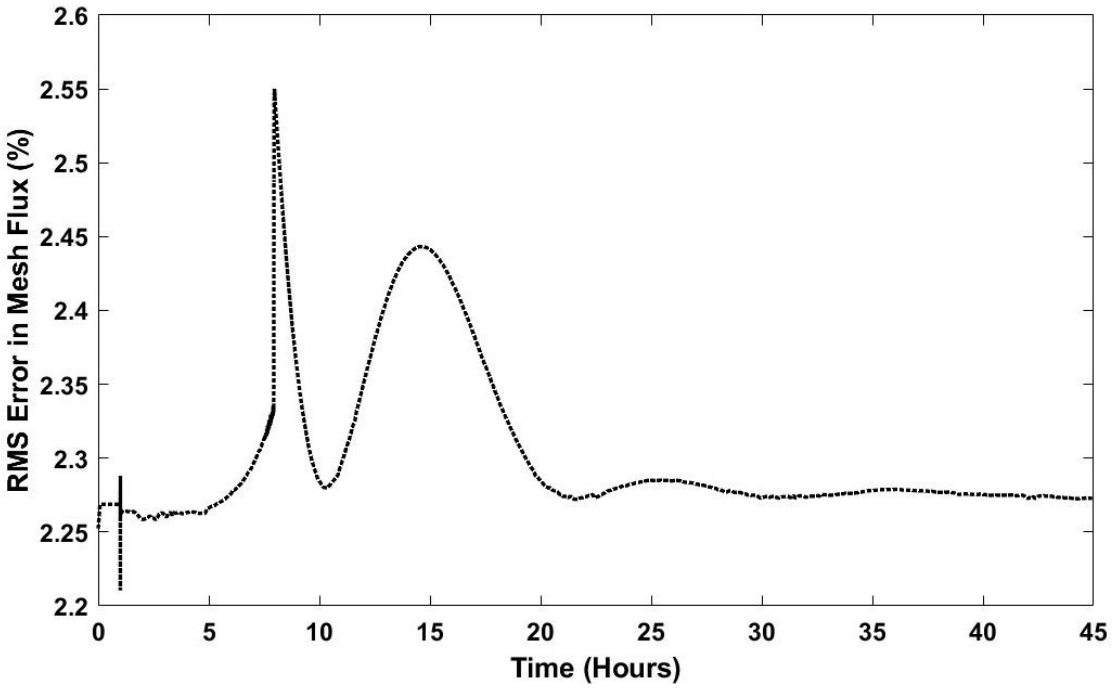

Fig. 19. Variation of ε_{RMS} with time during xenon spatial oscillations

Table. 1(A) Maximum value of ε_{RMS} and its time of occurrence during movement of one or multiple RRs

Operational scenario	**Maximum value of ε_{RMS} (%)**	**Time at which the maximum ε_{RMS} occurs (Seconds)**
Movement of RR-1	2.40	40
In-phase Movement of RRs 1 and 3	2.37	45
In-phase Movement of RRs 1 and 5	2.44	40
In-phase Movement of RRs 1 and 7	2.37	46
In-phase Movement of RRs 3 and 5	2.37	46
In-phase Movement of RRs 3 and 7	2.38	47
In-phase Movement of RRs 5 and 7	2.37	45
In-phase Movement of RRs 1, 3 and 5	2.38	46
In-phase Movement of RRs 3, 5 and 7	2.35	46
In-phase Movement of RRs 5, 7 and 1	2.38	47
In-phase simultaneous movement of RRs 1, 3, 5 and 7	2.36	45
Out-of-phase Movement of RRs 1 and 3	2.42	21
Out-of-phase Movement of RRs 1 and 5	2.36	19
Out-of-phase simultaneous movement of RRs 1 and 3 and RRs 5 and 7	2.35	25
Out-of-phase simultaneous movement of RRs 1 and 5 and RRs 3 and 7	2.41	23

Table. 1(B) Maximum value of ε_{MAE}, time of its occurrence and location and frequency distribution of ε_{MAE} during movement of one or multiple RRs

Operational scenario	**Maximum value of ε_{MAE} (%)**	**Location**	**Time instant of occurrence (Seconds)**	**Frequency distribution of ε_{MAE}**		
				ε_{MAE}< 2.5%	**2.5%≤ ε_{MAE}<5 %**	**ε_{MAE}≥5 %**
Movement of RR-1	7.29	C,19, 8	43	71.78	25.77	2.45
In-phase Movement of RRs 1 and 3	6.36	F,13, 8	45	72.32	25.58	2.10
In-phase Movement of RRs 1 and 5	6.58	X, 7, 8	43	71.60	25.77	2.63
In-phase Movement of RRs 1 and 7	6.46	F,13, 8	39	72.01	26.06	1.93
In-phase Movement of RRs 3 and 5	6.46	U,13, 8	39	72.01	26.06	1.93
In-phase Movement of RRs 3 and 7	6.50	U,13, 8	40	72.20	25.76	2.05
In-phase Movement of RRs 5 and 7	6.36	U,13, 8	45	72.32	25.57	2.11
In-phase Movement of RRs 1, 3 and 5	6.31	U,13, 8	44	72.22	25.64	2.15
In-phase Movement of RRs 3, 5 and 7	6.38	U,13, 8	39	72.29	25.89	1.82
In-phase Movement of RRs 5, 7 and 1	6.31	F,13, 8	44	72.22	25.64	2.15
In-phase simultaneous movement of RRs 1, 3, 5 and 7	6.29	F,13, 8	35	71.75	26.17	2.08
Out-of-phase Movement of RRs 1 and 3	7.29	C,19, 7	21	70.80	26.57	2.64
Out-of-phase Movement of RRs 1 and 5	6.94	C,19, 7	19	72.25	25.41	2.34
Out-of-phase simultaneous movement of RRs 1 and 3 and RRs 5 and 7	6.19	F,13, 7	25	72.10	25.90	2.00
Out-of-phase simultaneous movement of RRs 1 and 5 and RRs 3 and 7	6.46	C,19, 7	25	70.91	26.70	2.40

Table 2(A) Maximum value of ε_{RMS} and its time of occurrence during refuelling of a coolant channel in the zones

Operational scenario	**Maximum value of ε_{RMS} (%)**	**Time at which the maximum ε_{RMS} occurs (Minutes)**
Refuelling of a coolant channel in zone 1	4.45	285
Refuelling of a coolant channel in zone 2	2.34	64
Refuelling of a coolant channel in zone 3	3.28	44
Refuelling of a coolant channel in zone 10	3.93	44
Refuelling of a coolant channel in zone 11	3.59	44

Table. 2(B) Maximum value of ε_{MAE}, time of its occurrence and location and frequency distribution of ε_{MAE} during refuelling of a coolant channel in the zones

Operational scenario	**Maximum value of ε_{MAE} (%)**	**Location**	**Time instant of occurrence (Minutes)**	**Frequency distribution of ε_{MAE}**			
				ε_{MAE} < 2.5%	**2.5% ≤ ε_{MAE} <5%**	**5%≤ ε_{MAE}<7.5%**	**ε_{MAE} ≥7.5 %**
Refuelling of a coolant channel in zone 1	13.43	C,7,7	285	53.54	27.54	11.80	7.13
Refuelling of a coolant channel in zone 2	6.1	U, 13, 8	28	72.47	25.92	1.60	0.00
Refuelling of a coolant channel in zone 3	15.2	J,24,10	43	71.78	25.77	2.45	0.00
Refuelling of a coolant channel in zone 10	16.78	D,20,9	43	60.06	27.37	7.72	4.86
Refuelling of a coolant channel in zone 11	16.34	C,19,9	41	63.50	26.54	6.77	3.19

Table. 3 Maximum value of ε_{MAE}, time of its occurrence and location and frequency distribution of ε_{MAE} during xenon spatial oscillations

Operational scenario	$\boldsymbol{\varepsilon_{MAE}}$ **(%)**	**Location**	**Time instant of occurrence (Hours)**	**Frequency distribution of $\boldsymbol{\varepsilon_{MAE}}$**		
				$\boldsymbol{\varepsilon_{MAE}}$**< 2.5%**	**2.5%≤ $\boldsymbol{\varepsilon_{MAE}}$<5%**	$\boldsymbol{\varepsilon_{MAE}}$**≥ 5%**
Xenon spatial oscillation	9.03	C, 19, 8	7.97	70.80	25.49	3.71

Bibliography:

Ananthoju, R., Tiwari, A.P., Belur, M.N., 2016. A Two-Time-Scale Approach for Discrete-Time Kalman Filter Design and Application to AHWR Flux Mapping. IEEE Trans. Nucl. Sci. 63, 359–370. https://doi.org/10.1109/TNS.2015.2500917

Anupreethi, B., Gupta, A., Kannan, U., Tiwari, A.P., 2020. Optimization of flux mapping in-core detector locations in AHWR using clustering approach. Nucl. Eng. Des. 366, 110756. https://doi.org/10.1016/j.nucengdes.2020.110756

Anupreethi, B., Gupta, A., Kannan, U., Tiwari, A.P., 2019. Computation of Higher Eigenmodes using Subspace iteration scheme and its application to Flux Mapping System of AHWR, in: International Conference on Advances in Energy Research - ICAER. IIT Mumbai, India.

Ezure, H., 1988. Estimation of most probable power distribution in BWRs by least squares method using in-core measurements. J. Nucl. Sci. Technol. 25, 731–740. https://doi.org/10.1080/18811248.1988.9735917

Gupta, A., 2012. A 3D Space-Time Analysis Code in Cartesian and Hexagonal Geometries, in: National Symposium on Radiation Physics (NSRP-19). Mamallapuram, Tamilnadu.

Hinchley, E., Kugler, G., 1974. On-line control of the CANDU-PHW power distribution, in: IAEA Specialists Meeting on Spatial Control Problems. Studsvik, Sweden.

Kim, B.G., Kim, I.S., Kim, S.Y., 1991. Core Simulations Using Actual Detector Readings for a Canada Deuterium Uranium Reactor. Nucl. Technol. 93, 138–146. https://doi.org/10.13182/NT91-A34500

Lee, K., Kim, C.H., 2003. The Least-Squares Method for Three-Dimensional Core Power Distribution Monitoring in Pressurized Water Reactors. Nucl. Sci. Eng. 143, 268–280. https://doi.org/10.13182/NSE03-A2335

Li, W., Ding, P., Duan, C., Cui, D., Qiu, R., Shi, X., Lin, J., 2019. Comparison of three methodologies for optimization of the layout of in-core detectors with a specific number of detectors. Ann. Nucl. Energy 126, 359–366. https://doi.org/10.1016/j.anucene.2018.11.039

Mishra, A.K., Shimjith, S.R., Bhatt, T.U., Tiwari, A.P., 2013. Dynamic compensation of vanadium self powered neutron detectors for use in reactor control. IEEE Trans. Nucl. Sci. 60, 310–318. https://doi.org/10.1109/TNS.2012.2229719

Mishra, S., Modak, R.S., Ganesan, S., 2012. Computational Schemes for Online Flux Mapping System in a Large-Sized Pressurized Heavy Water Reactor. Nucl. Sci. Eng. 170, 280–289. https://doi.org/10.13182/NSE10-84

Modak, R.S., Jain, V.K., 1996. Sub-space iteration scheme for the evaluation of λ-modes of finite-differenced multi-group neutron diffusion equations. Ann. Nucl. Energy 23, 229–237. https://doi.org/10.1016/0306-4549(95)00015-6

Peng, X., Wang, K., Li, Q., 2014. A new power mapping method based on ordinary kriging and determination of optimal detector location strategy. Ann. Nucl. Energy 68, 118–123.

https://doi.org/10.1016/j.anucene.2014.01.002

Razak, R.A., Bhushan, M., Belur, M.N., Tiwari, A.P., Kelkar, M.G., 2014. Clustering of Self Powered Neutron Detectors : Combining Prompt and Slow Dynamics. IEEE Trans. Nucl. Sci. 61, 3635–3643. https://doi.org/10.1109/TNS.2014.2366931

Saad, Y., 2011. Numerical methods for large Eigenvalue problems. Minneapolis.

Shimjith, S.R., Tiwari, A.P., Bandyopadhyay, B., 2013. Modeling and Control of a Large Nuclear Reactor. Springer-Verlag Berlin Heidelberg. https://doi.org/10.1007/978-3-642-30589-4

Shimjith, S.R., Tiwari, A.P., Naskar, M., Bandyopadhyay, B., 2010. Space-time kinetics modeling of Advanced Heavy Water Reactor for control studies. Ann. Nucl. Energy 37, 310–324. https://doi.org/10.1016/j.anucene.2009.12.011

Sinha, R.K., Kakodkar, A., 2006. Design and development of the AHWR — the Indian thorium fuelled innovative nuclear reactor. Nucl. Eng. Des. 236, 683–700. https://doi.org/10.1016/j.nucengdes.2005.09.026

Stacey, W.M., 2007. Nuclear Reactor Physics, Wiley-VCH Verlag GmbH & Co. KGaA. https://doi.org/10.1002/9783527611041

Terman, M.S., Kojouri, N.M., Khala, H., 2018. Optimal placement of fixed in-core detectors for Tehran Research Reactor using information theory. Prog. Nucl. Energy 106, 300–315. https://doi.org/10.1016/j.pnucene.2018.03.012

Xia, L., Jiang, J., Javidnia, H., Luxat, J.C., 2012. Performance evaluation of a 3-D kinetic model for CANDU reactors in a closed-loop environment. Nucl. Eng. Des. 243, 76–86. https://doi.org/10.1016/j.nucengdes.2011.11.034

Yellapu, V.S., Tiwari, A.P., Degweker, S.B., 2017. Application of data reconciliation for

fault detection and isolation of in-core self-powered neutron detectors using iterative principal component test. Prog. Nucl. Energy 100, 326–343. https://doi.org/10.1016/j.pnucene.2017.04.017

Yellapu, V.S., Tiwari, A.P., Shimjith, S.R., Naskar, M., Degweker, S.B., 2013. Space-time kinetics modeling for the determination of neutron detector signals in Advanced Heavy Water Reactor. Proc. IEEE Int. Conf. Control Appl. 1224–1229. https://doi.org/10.1109/CCA.2013.6662919